

Journal of Geophysical Research: Atmospheres

RESEARCH ARTICLE

10.1002/2014JD022244

Key Points:

- Polar winter MILs in WACCM and observations show a maximum frequency near 180°E
- Midlatitude winter MILs tend to occur above anticyclones
- Midlatitude winter MILs occur as a result of planetary wave decay

Correspondence to:J. A. France,
jeffrey.france@colorado.edu**Citation:**France, J. A., V. L. Harvey, C. E. Randall, R. L. Collins, A. K. Smith, E. D. Peck, and X. Fang (2015), A climatology of planetary wave-driven mesospheric inversion layers in the extratropical winter, *J. Geophys. Res. Atmos.*, 120, 399–413, doi:10.1002/2014JD022244.

Received 1 JUL 2014

Accepted 8 DEC 2014

Accepted article online 11 DEC 2014

Published online 19 JAN 2015

Corrected 29 JUL 2015

This article was corrected on 29 JUL 2015. See the end of the full text for details.

A climatology of planetary wave-driven mesospheric inversion layers in the extratropical winter

J. A. France¹, V. L. Harvey^{1,2}, C. E. Randall^{1,2}, R. L. Collins³, A. K. Smith⁴, E. D. Peck^{1,2}, and X. Fang¹

¹Laboratory for Atmospheric and Space Physics, University of Colorado Boulder, Boulder, Colorado, USA, ²Department of Atmospheric and Oceanic Sciences, University of Colorado Boulder, Boulder, Colorado, USA, ³Geophysical Institute and Department of Atmospheric Sciences, University of Alaska Fairbanks, Fairbanks, Alaska, USA, ⁴National Center for Atmospheric Research, Boulder, Colorado, USA

Abstract Mesospheric inversion layers (MILs) are a useful diagnostic to simultaneously investigate middle atmosphere radiation, chemistry, and dynamics in high-top general circulation models. Climatologies of long-lived extratropical winter MILs observed by the Microwave Limb Sounder (MLS) and the Sounding of the Atmosphere using Broadband Emission Radiometry (SABER) satellite instruments are compared to MILs in the Whole Atmosphere Community Climate Model (WACCM). In general, MIL location, amplitude, and thickness statistics in WACCM are in good agreement with the observations, though WACCM middle- and high-latitude winter MILs occur 30%–50% more often than in MLS and SABER. This work suggests that planetary wave-driven MILs may form as high as 90 km. In the winter, MILs display a wave-1 pattern in both hemispheres, forming most often over the region where the climatological winter stratospheric anticyclones occur. These MILs are driven by the decay of vertically propagating planetary waves in the mesospheric surf zone in both observations and in the model. At the base of polar inversions there is climatological local ascent and cooling situated atop the stratospheric anticyclones, which enhances the cold base of the MILs near 60 km and 120°E longitude.

1. Introduction

While the lapse rate is generally positive in the mesosphere (decreasing temperatures with height), it is common for there to be regions of negative lapse rate. These are known as mesospheric inversion layers (MILs) and are caused by the interaction of waves, tides, and the mean flow. MILs were first observed by Schmidlin [1976], who used a variety of in situ measurement techniques to document and verify a MIL near 75 km. Since then, MILs have been extensively documented using in situ and satellite temperature data and are known to be climatological features in the mesosphere-lower thermosphere, persisting for days and spanning thousands of square kilometers [e.g., Meriwether and Gerrard, 2004; Gan *et al.*, 2012].

Meriwether and Gerrard [2004] identified two distinct classifications of MILs: the upper MIL, occurring between 85 km and 100 km, and the lower MIL, which occurs below 80 km. Studies by Liu and Hagan [1998], Liu *et al.* [2000], and States and Gardner [2000] concluded that upper MILs result from the interaction of gravity waves with tides. Liu and Hagan [1998] and Liu *et al.* [2000] used numerical simulations to quantify the role of gravity waves and tides on MIL formation. Liu *et al.* [2000] found that gravity wave-driven turbulent eddy diffusion heating and cooling rates of up to 10 K/h are possible at the lower and upper edge of the breaking region, respectively, and that these anomalies are transient and strongly dependent on the diurnal tide. The resulting temperature anomalies are consistent with the observed magnitude of MILs. Other mechanisms that may also play a role in the formation of MILs are mechanical heating by gravity wave breaking [Hauchecorne *et al.*, 1987], nonlinear interactions between gravity waves and tides [Meriwether and Gardner, 2000], planetary waves (PWs) and gravity waves [Irving *et al.*, 2014], and chemical heating [Meriwether and Mlynczak, 1995; Ramesh *et al.*, 2013]. Meriwether and Mlynczak [1995] used a two-dimensional model to show that chemical heating rates between 80 km and 95 km may be as large as 3–10 K/d. While this likely leads to the formation of some MILs, it is insufficient to explain the 20–30 K MIL amplitudes frequently observed, particularly at middle to high latitudes where there is significant turbulent mixing and vertical transport. More recently, Ramesh *et al.* [2013] combined Sounding of the Atmosphere using Broadband Emission Radiometry (SABER) data and Rayleigh lidar observations at 13.5°N and 79.2°E to show a few cases in January and February 2011 in which large MILs

formed in the presence of weak gravity wave forcing. They concluded that these MILs occurred as a result of exothermic chemical reactions between atomic hydrogen and ozone, leading to heating rates of 15 K/d between 80 km and 85 km.

The ability to simulate MILs accurately in high-top models thus depends on the simulations of both the background temperature field and wave-mean flow interactions. Planetary and gravity waves are the primary mechanism by which energy and momentum are transported upward from the troposphere. Where waves break and deposit their energy and momentum is important for understanding vertical coupling in the atmosphere. In fact, PW filtering of gravity waves, the location of the critical line, and the formation of MILs are intimately linked [Smith 1996; 2003; Sassi *et al.*, 2002]. Since MILs are a manifestation of breaking waves [e.g., Collins *et al.*, 2011], we can use them to understand how and where energy and momentum are being deposited into the middle atmosphere, improving our understanding of the wave-driven global residual circulation [e.g., Haurwitz, 1961; Hitchman *et al.*, 1989], including the downward transport of NO_x from the mesosphere to the stratosphere in the polar winter [e.g., Randall *et al.*, 2006; 2009]. MILs also have a significant effect on atmospheric stability. An inversion layer leads to higher stability below the top of the inversion, resulting in reduced vertical transport and mixing [e.g., Wallace and Hobbs, 1977; Salby, 1996]. The region above the temperature maximum is characterized by a lapse rate that is close to adiabatic [Whiteway *et al.*, 1995; Duck *et al.*, 2001], reduced stability, enhanced mixing and vertical transport [Sica *et al.*, 2007], and strong eddy diffusion [Collins *et al.*, 2011].

MILs have long been observed in the lidar record [e.g., Hauchecorne *et al.*, 1987; Dao *et al.*, 1995; Leblanc and Hauchecorne, 1997; Meriwether *et al.*, 1998; States and Gardner, 1998; Cutler *et al.*, 2001; Duck *et al.*, 2001; Kumar *et al.*, 2001; Duck and Greene, 2004; Irving *et al.*, 2014]. One of the earliest MILs documented is reported by Hauchecorne *et al.* [1987], who used lidar data at Biscarrosse, France, to observe the evolution of a MIL between 75 km and 80 km that persisted for 5 days beginning on 1 December 1986. With daily global satellite temperature profiles we can now examine the spatial and temporal characteristics of MILs. Gan *et al.* [2012] used Sounding of the Atmosphere using Broadband Emission Radiometry (SABER) temperatures to produce a global climatology of MILs. They demonstrated that MILs occur at all latitudes with strong seasonal dependencies. In particular, they showed that tropical MILs have maximum frequencies at equinox and are associated with the mesospheric semiannual oscillation.

Salby *et al.* [2002] developed a theory to explain the mechanism by which PWs lead to MILs. They showed that the lapse rate is inversely proportional to the second derivative (curvature) of the geopotential (Φ) with altitude (see their equation (3)). Dividing the lapse rate and geopotential into mean and wave-driven (eddy) components, they argued that if the eddy geopotential vertical curvature was large enough, then a MIL would form. Sassi *et al.* [2002] used the Whole Atmosphere Community Climate Model (WACCM) to show a year of MIL statistics at 43°N and 0°E. Their results indicate that MILs at this location are best defined between December and February, with daily MIL amplitudes generally between 10 K and 40 K and MIL base heights between 65 km and 75 km (see their Figure 2). They showed a representative model day to illustrate that a MIL formed above positive stratospheric geopotential anomalies (see their Figure 4) and conclude that midlatitude MILs result from the rapid decay with height of vertically propagating PWs. While the positive anomalies on this particular day were centered near 90°E, positive geopotential anomalies are climatologically situated roughly over the Aleutian archipelago [e.g., Harvey and Hitchman, 1996].

In this work, we extend the work of Sassi *et al.* [2002] by documenting the climatological geographical distribution of MIL occurrence frequency using 40 years of free-running WACCM and by explicitly demonstrating the mechanism proposed by Salby *et al.* [2002] and discussed by Sassi *et al.* [2002]. We compare long-lived MILs in WACCM to MILs observed by SABER and the Aura Microwave Limb Sounder (MLS) satellite instruments. Section 2 describes WACCM, SABER, MLS, meteorological analyses, and the analysis methods used. Section 3 presents the MIL climatology. In section 4 we explore the mechanisms driving MIL formation in the polar winter. Specifically, we consider the role of wave-driven ascent and cooling below the gravity wave-driven mesospheric surf zone as well as decaying PWs in the formation and enhancement of MILs. Conclusions are given in section 5.

2. Global Model, Satellite Data, and Analysis Methods

2.1. WACCM

The National Center for Atmospheric Research (NCAR) Whole Atmosphere Community Climate Model version 4 (WACCM4) in the Community Earth System Model version 1.0.4 framework is a global general circulation

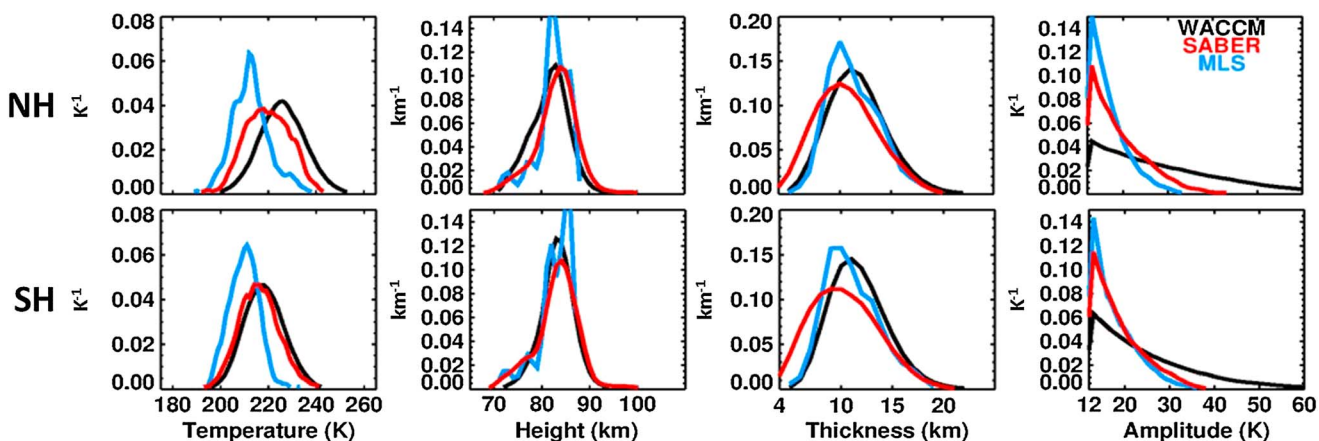


Figure 1. Frequency per unit of MIL (first column) maximum temperature, (second column) altitude, (third column) thickness, and (fourth column) amplitude (top row) between 50°N and 60°N from 15 January to 15 March and (bottom row) between 50°S and 60°S from 15 July to 15 September. MILs in WACCM are black, SABER MILs are red, and MLS MILs are blue. Frequencies include 40 years of WACCM output, 12 years of SABER data (2002–2014), and 10 years of MLS data (2004–2014).

model extending from the surface to about 145 km [Garcia et al., 2007]. The horizontal resolution is 1.9° latitude by 2.5° longitude, with 66 pressure levels between the surface and the lower thermosphere, and a vertical resolution of ~3.5 km above 65 km. Net heating rates are interpreted as diabatic vertical velocities in isentropic coordinates and represent the sum of all shortwave heating and longwave cooling processes. WACCM simulates with a finite volume dynamical core from the NCAR Community Atmosphere Model version 4 developed for the NCAR Community Climate System Model version 4 [Gent et al. 2011; Lin, 2004]. The physics in WACCM are based on the NCAR Community Climate Model, version 3 (CCM3) [Kiehl et al., 1996], and transport is determined from the explicit flux-form semi-Lagrangian advection scheme of Lin and Rood [1997]. Chemistry in WACCM is from the Model for Ozone and Related Chemical Tracers version 3 [Brasseur et al., 1998; Kinnison et al., 2007] and is fully coupled with the dynamics. Gravity wave parameterizations include wave generation by convection [Beres et al., 2005], fronts [Richter et al., 2010], and flow over topography [McFarlane, 1987]; the model also includes turbulent mountain stress due to unresolved orography [Richter et al., 2010]. WACCM has been shown to simulate a realistic Northern Hemisphere (NH) winter stratosphere [De La Torre et al., 2012; Chandran et al., 2013] and global stratopause [France and Harvey, 2013], capturing PW-driven zonal asymmetries in stratopause height and temperature. Relative to SABER, WACCM shows a significant bias in the mesospheric lapse rate [see Smith, 2012, Figure 1] that likely influences our results. In particular, the WACCM temperature at the mesopause is warmer than observed, so the lapse rate in the upper mesosphere is lower. Therefore, a temperature perturbation can more easily reverse the gradient from negative to positive. So while we expect higher MIL occurrence frequencies in WACCM, the model is still useful for the climatology analysis we produce here. We use 40 years of daily averaged temperature, geopotential height, horizontal wind, and net diabatic heating rates in our analysis. WACCM was run with repeating year 2000 A.D. conditions and prescribed ocean sea surface temperatures as described in Hurrell et al. [2008].

2.2. Modern-Era Retrospective Analysis for Research and Applications

For comparison to WACCM, the Modern-Era Retrospective Analysis for Research and Applications (MERRA) [Rienecker et al., 2011] is used to characterize the large-scale temperature and wind fields and to identify the stratospheric polar vortices and anticyclones [Harvey et al., 2002]. MERRA extends into the mesosphere, though, as is typical with reanalysis models, it has deficiencies at high altitudes due to a lack of observations above the middle stratosphere and limitations of gravity wave parameterizations [Rienecker et al., 2011]. The horizontal resolution of MERRA data is 0.5° latitude by 0.67° longitude with 72 vertical levels from the surface to 0.01 hPa. The vertical resolution of MERRA is ~2 km in the upper stratosphere and lower mesosphere. MERRA includes orographic gravity wave drag based on McFarlane [1987] as well as nonorographic waves based on Garcia and Boville [1994].

2.3. MLS

The MLS instrument was launched on 15 July 2004 on board NASA's Earth Observing System Aura satellite [Waters et al., 2006] into a Sun-synchronous polar orbit. MLS measures thermal microwave emissions from the

Earth's limb between 82°S and 82°N, providing about 3500 vertical profiles each day. Temperature is inferred from emission of oxygen at 118 GHz [Livesey *et al.*, 2013]. The temperature measurements have a vertical resolution of ~6 km in the mesosphere and are considered useful to 0.001 hPa. The temperature precision is ~2.3 K at 0.01–0.001 hPa, as inferred from coincident comparisons with eight correlative data sets [Schwartz *et al.*, 2008; Livesey *et al.*, 2013]. Uncertainty due to noise and a priori information is 2.5 K in the mesosphere. Data are filtered using version 3 status, quality, threshold, and convergence values provided by the MLS science team [Livesey *et al.*, 2013].

2.4. SABER

SABER was launched on board the Thermosphere Ionosphere Mesosphere Energetics and Dynamics (TIMED) satellite on 7 December 2001 into a 625 km circular orbit with an inclination of 74.1° [Russell *et al.*, 1999]. SABER samples along track every ~300 km providing coverage from 52°S to 83°N, or from 83°S to 52°N, depending on the orientation of TIMED. The coverage alternates every ~60 days due to yaw maneuvers of TIMED that rotate the SABER view direction by 180°. SABER data products are linearly interpolated onto 201 geometric altitude levels ranging from 0 km to 200 km in 1 km increments. The vertical resolution of SABER is 2–3 km [Mertens *et al.*, 2001]. This work uses version 2.0 kinetic temperature and derived geopotential height as a function of pressure provided in the L2A data files obtained from <http://saber.gats-inc.com/>. Kinetic temperature is determined from the 15 μm and 4.3 μm bands of CO₂ with the assumptions that CO₂ has a well-known volume mixing ratio. Remsberg *et al.* [2008] compared the SABER version 1.07 temperatures to data from the Michelson Interferometer for Passive Atmospheric Sounding and Rayleigh lidar profiles for the upper stratosphere and lower to middle mesosphere and found that SABER has a 1 K cold bias near the stratopause. They determined the projected error for SABER in the upper stratosphere and lower mesosphere from systematic and random errors to be 2 K.

2.5. Analysis Methods

Temperature data from MLS and SABER are interpolated to a 2.5° latitude by 3.75° longitude grid using a Delaunay triangulation at each vertical level, and the data are linearly interpolated to a vertical grid with 1 km resolution. MILs are identified using daily averaged gridded temperature profiles and the method of Gan *et al.* [2012]. Our upper boundary is 100 km instead of 85 km, in order to flag more upper MILs. MILs are defined as follows:

1. For each grid point, a 3 day running mean temperature profile is calculated in order to identify only robust, long-lasting MILs.
2. Local temperature maxima and minima are identified between 65 km and 100 km for each vertical profile, requiring each maximum to be warmer and each minimum to be colder than the adjacent four vertical levels.
3. When a local temperature maximum occurs above a local temperature minimum, and the difference between an adjacent temperature maximum and minimum in thickness and amplitude is greater than 4 km and 12 K, respectively, a MIL is identified.
4. The altitude of the MIL is defined at the altitude of the local maximum, and the base is the altitude of the local minimum.

These thresholds are consistent with previous work [Leblanc and Hauchecorne, 1997; Fechene *et al.*, 2008; Gan *et al.*, 2012] and close to the vertical resolution of WACCM in the mesosphere. We define thickness as the vertical distance over which the profile has a negative lapse rate. Amplitude is defined as the difference in temperature between the top and bottom of the inversion layer. The temperature of the MIL is defined at the top of the inversion.

Since tidal variability in temperature can be large in the mesosphere [e.g., Wu *et al.*, 2008; Xu *et al.*, 2009; Mukhtarov *et al.*, 2009], tides are removed from the observations and the model data in the following way: WACCM output is daily averaged and MLS profiles are averaged over ascending and descending orbits. For SABER, we fit a sine wave to the temperature at each latitude and vertical level as a function of local time, over each 60 day yaw period. We then subtract the local time-dependent tidal amplitude from each temperature measurement. One of the shortcomings of removing the tides in this way is that variations in zonal mean temperature during the precession period are assumed to be tidally induced, as noted by Zhang *et al.* [2006].

3. MIL Climatology

The work presented here focuses on middle- to high-latitude MILs during the winter months and the zonal asymmetries in their geographic distributions. Figure 1 compares WACCM and observed occurrence frequency per unit of MIL temperature (first column), altitude (second column), thickness (third column), and amplitude (fourth column) from 50°N to 60°N during 15 January to 15 March (top row) and from 50°S to 60°S during 15 July to 15 September (bottom row). These time periods are chosen based on the dates of the SABER yaw maneuver, which prevents us from considering December in the NH and June in the Southern Hemisphere (SH). There is reasonable agreement in all parameters, but with some significant differences. MIL temperatures in the NH peak at 212 K, 218 K, and 226 K and in the SH at 211 K, 215 K, and 217 K in MLS, SABER, and WACCM, respectively. While these are in relatively good agreement, the width of the MLS distribution is significantly smaller than that of the SABER or WACCM distributions, possibly because of the coarser vertical resolution of MLS.

MIL altitudes are in excellent agreement, peaking in the NH at 82 km, 84 km, and 83 km and in the SH at 84 km, 85 km, and 83 km in MLS, SABER, and WACCM, respectively. MILs are commonly divided into lower and upper MILs, with lower MILs occurring below 80 km and upper MILs occurring between 85 and 100 km [Meriwether and Gerrard, 2004]. Note that we do not see a strong bimodal distribution with maxima in each of the upper and lower MIL regimes. Instead, our results show a large population of MILs at an altitude between these two regimes. This is likely because we remove the diurnal tides and consider only long-lived, large-amplitude MILs, which would prevent us from identifying the upper MIL described by Meriwether and Gerrard [2004]. This result suggests that PW-driven MILs are distributed continuously between ~70 km and ~90 km.

MIL thicknesses (third column) for the middle to high latitude, wintertime data are on average between 9 km and 11 km in all three data sets, with the thickest inversions approaching 20 km. This is in agreement with Gan *et al.* [2012], who showed that MILs at high latitudes are thicker on average than at any other latitudes. All three data sets show a maximum amplitude at the 12 K lower limit set by our definition of a MIL. The distribution of MIL amplitudes is broader in WACCM than in either SABER or MLS. WACCM amplitudes reach 60 K, whereas the maximum observed amplitude is 40 K in SABER and 35 K in MLS. This is likely a result of the background temperatures in WACCM decreasing too slowly in the mesosphere [Sica *et al.*, 2007; Smith, 2012], resulting in less energy needed to reverse the lapse rate and form a large-amplitude MIL.

Figure 2 shows the frequency of occurrence of MILs in WACCM (top row), SABER (middle row), and MLS (bottom row) from 15 November to 15 January (left column) and 15 January to 15 March (right column) in the NH. The winter is divided into these two periods based on the date of the SABER yaw maneuver. Frequency is determined by MIL counts per grid point divided by the total number of days considered. The thick black contour denotes regions where the polar vortex is present more than 60% of the time at 50 km, and anticyclones are present at least 60% of the time at 50 km equatorward of the thick gray contour. There is 30–50 km of vertical separation between the vortex/anticyclones at 50 km and the MILs in the mesosphere. Gan *et al.* [2012] showed SABER MILs in this way for individual days in December. We expand upon their work by using MLS to augment the data from the southward looking yaw periods of SABER. We also show late winter when SABER is looking toward the Arctic. This figure highlights that polar winter MILs often form above the climatological stratospheric anticyclones in the mesospheric surf zone. The maximum in MIL frequency occurs between the poleward edge of the Aleutian High and the vortex in MLS and directly above the stratospheric anticyclone in WACCM. The maximum MIL frequencies of 50–60% in WACCM over the North Pacific are similar to the frequencies reported by Irving *et al.* [2014] who identified MILs in lidar measurements at Chathanika, Alaska, 55%, 62%, and 68% of the time in November, December, and January, respectively. In both WACCM and observations, MILs rarely form above the polar vortices. These results are consistent with Sassi *et al.* [2002], who demonstrated that MILs occur above the region of positive geopotential anomalies and attributed MIL formation to the decay and dissipation of PWs with height, causing MILs to form in the mesospheric surf zone where zonal winds are weak. They also ruled out the semidiurnal tide and gravity wave filtering as dominant mechanisms. Due to the quasi-stationary character of PWs, they hypothesized that maximum MIL frequency would occur in the eastern hemisphere. While our results agree with Sassi *et al.* [2002] in that MILs occur over the positive geopotential anomalies, we find that the frequency is greatest over the climatological Aleutian High near ~180°E rather than near 90°E, though MLS does show a secondary maximum near 90°E. The difference is likely because their work focused on 43°N, and the peak in MIL frequency we see is near 55°N.

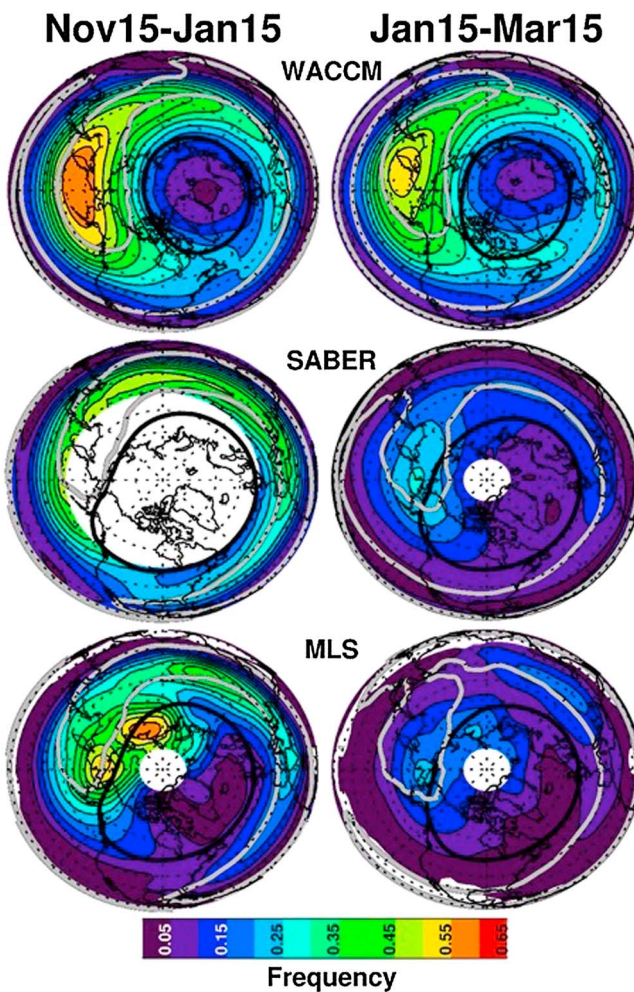


Figure 2. NH polar projections of mean MIL frequency for (top row) WACCM, (middle row) SABER, and (bottom row) MLS in the NH (left column) between 15 November and 15 January and (right column) between 15 January and 15 March. Means include 40 years of WACCM output, 12 years of SABER data (2002–2014), and 10 years of MLS data (2004–2014). The Greenwich Meridian is oriented to the right. The thick black and gray contours enclose the regions where the vortex and anticyclone are present at 50 km at least 60% of the time. Frequencies are based on the total number of MILs identified at each grid point divided by the number of days in each record.

during 15 July to 15 September. The differences in frequency plotted are to better illustrate the increased PW amplitudes late in the season, which leads to more frequent middle- to high-latitude anticyclones and vortex displacement. There are a number of differences between WACCM and observations in SH MIL frequency. In general, WACCM simulates much higher MIL frequencies than observed. In early winter, maximum WACCM frequencies are shifted in longitude by 90° or more from observed. Also, WACCM shows much higher frequencies in late winter than in early winter, while both SABER and MLS show a decrease in frequencies in late winter.

In both early and late winter, MILs in WACCM occur most often poleward of Australia, with a maximum frequency of occurrence near ~40% in early to middle winter. Unlike in the NH, the anticyclones and MILs in the observations are generally confined to latitudes equatorward of 30°S during early to middle winter; MLS shows a maximum frequency of only 10% poleward of 40°S. This is due to weaker PW forcing during early to middle SH winter. Since WACCM MILs are not confined to the lower latitudes, this suggests that PW forcing in WACCM is too strong in the SH early winter. In late winter, the vortex weakens, resulting in an increase in PW

From 15 November to 15 January (left column), MLS shows MILs forming poleward of those in WACCM, with a maximum occurrence between 60°N and 70°N. The maximum MIL frequency of occurrence during this time is ~60% in WACCM and MLS. SABER shows MILs occurring at a rate of ~50% at ~50°N, but observations do not extend further into the Arctic during this time of year. In late winter (right column), the maximum frequency of MILs is ~55% in WACCM, ~30% in SABER, and ~25% in MLS. Differences in polar MIL frequencies between WACCM and observations are likely related to differences in the strength of the PW forcing and a reduced background lapse rate in WACCM. Specifically, the polar vortex in WACCM is smaller than the polar vortex in MERRA at 50 km. The smaller vortex dimension is consistent with larger PW amplitudes, a larger mesospheric surf zone, and a larger area within which MILs form.

Figure 3 is the same as Figure 2 but for the SH from 15 May to 15 July (left column) and from 15 July to 15 September (right column). The latter is the period in which SABER is southward looking. Anticyclones are present at least 10% of the time equatorward of the thick gray contour during 15 May to 15 July and 30% of the time during 15 July to 15 September. Thick black contour encompasses regions where the vortex is present 30% of the time during 15 May to 15 July and 60% of the time

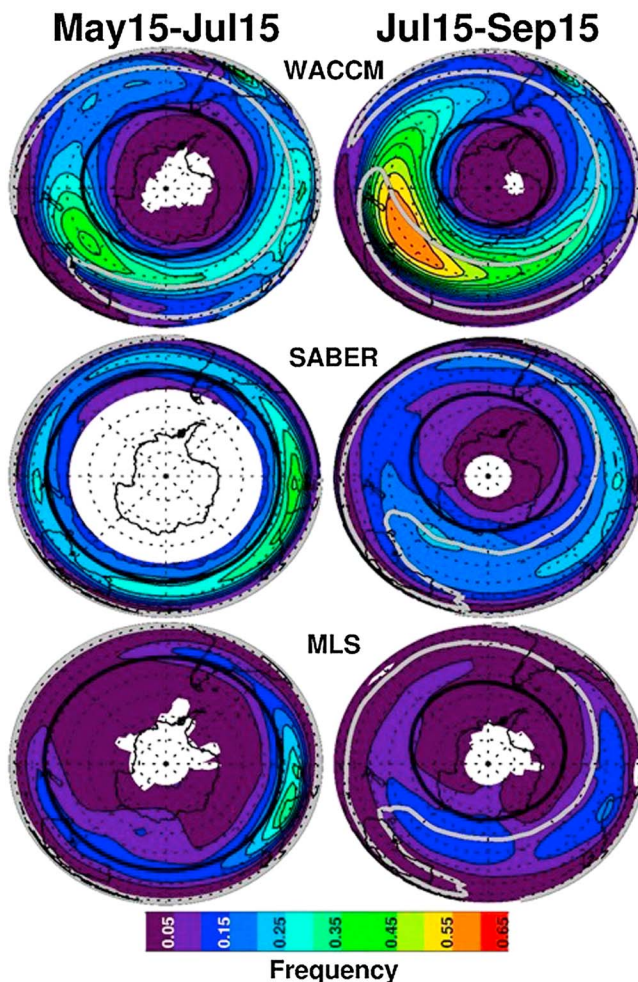


Figure 3. SH polar projections of mean MIL frequency for (top row) WACCM, (middle row) SABER, and (bottom row) MLS in the SH between (left column) 15 May and 15 July and (right column) 15 July and 15 September. Thick black contours are as in Figure 2. Anticyclones are present at least 10% of the time equatorward of the thick gray contour during 15 May to 15 July and 30% of the time during 15 July to 15 September. Thick black contour encompasses regions where the vortex is present 30% during 15 May to 15 July and 60% during 15 July to 15 September.

and early January. WACCM PWs in the NH are largest (~ 1600 m) in early December near 2 hPa and remain large throughout the season compared with observations. Largest differences between observed and modeled PW amplitudes occur in the SH (right column). SABER and MLS (middle and bottom rows) show an increase in PW amplitudes in July near 50 km, with maximum amplitudes descending to near 40 km in early September. WACCM also shows an increase in PW amplitudes in July, though they are generally a factor of 2 larger than the observations and do not descend with time. This figure shows that WACCM PW amplitudes are generally too large at both 50°N and 50°S. The overestimation of the PW amplitudes in WACCM likely contributes to the higher MIL frequencies in the model shown in Figure 3.

In order to further elucidate the relationship between PWs, vertical motions, and MILs, Figure 5 shows late winter MIL frequencies as a function of longitude and altitude at 55°N (left) and 50°S (right) in WACCM. The colors indicate the MIL occurrence frequency as a function of longitude and altitude; the altitude here corresponds to the base of the temperature inversion layer. Thick gray contours indicate the edge of the climatological stratospheric anticyclones. Thin black contours show $d\theta/dt$, which indicates diabatic vertical motion, with solid lines showing negative $d\theta/dt$, or diabatic descent, and dashed lines indicating positive

amplitudes, and anticyclones and MILs shifting poleward to between 50°S and 60°S and between 90°E and 180°E. WACCM also shows an increase in MILs poleward of 40°S. Maximum frequencies over the Australian High are about 60% in WACCM, 25% in SABER, and 15% in MLS. As in the NH, the Antarctic vortex in WACCM is smaller compared to the vortex in MERRA at 50 km and is likely a symptom of the strong PW forcing in WACCM.

Next we test our hypothesis that these MILs are driven by PWs, and differences in MIL frequencies between observations and WACCM are due to differences in PW amplitudes. Figure 4 shows PW-1 and PW-2 amplitudes derived from geopotential height from WACCM (top row), SABER (middle row), and MLS (bottom row) at 50°N (left column) and 50°S (right column). Thin black contours represent the fraction of days on which there was at least one MIL around the 50° latitude circle. In both hemispheres, observations show the maximum frequency of MILs occurring above the maxima in PW amplitudes. While MILs identified in WACCM occur fairly uniformly throughout both the NH and SH winters, it also shows an increase in MIL frequency with increasing PW amplitude. This is consistent with Irving et al. [2014] who showed that PW activity is a factor of 2 larger on days when MILs occur. SABER and MLS are in good agreement in the NH, with maximum wave amplitudes in the NH of ~ 1400 m occurring in late December

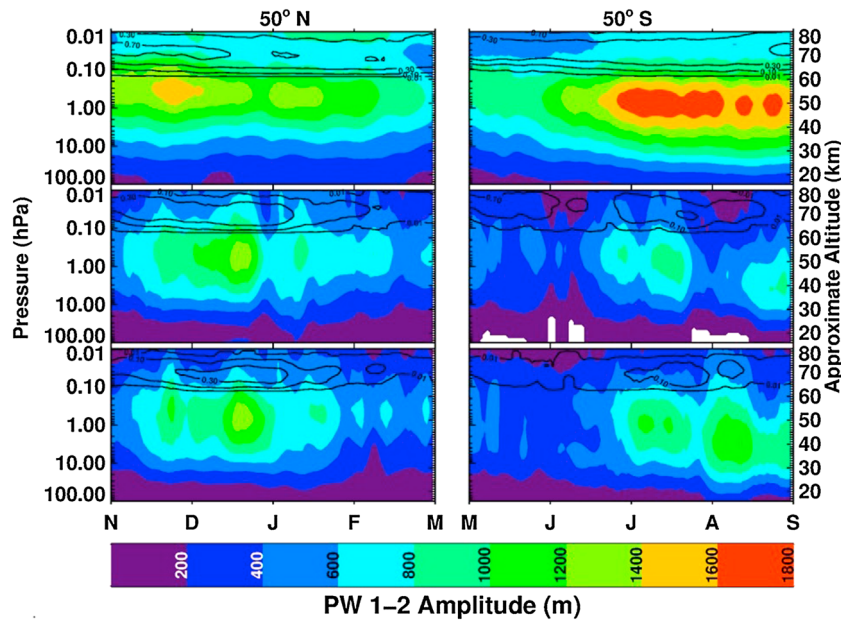


Figure 4. Pressure-time sections of PW-1 and PW-2 amplitudes for (top row) WACCM, (middle row) SABER, and (bottom row) MLS during winter at (left column) 50°N and (right column) 50°S. Thin black contours indicate the fractions of days over each data record on which there was at least one MIL identified somewhere around the 50° latitude circle, and indicate base altitude of the inversions. Month tick marks denote the fifteenth of each month.

$d\theta/dt$, or diabatic ascent, where θ is potential temperature. Positive $d\theta/dt$ indicates local ascent, because as air rises and cools, it becomes cold relative to the surrounding air and thus radiatively warms, resulting in increasing potential temperature, i.e., diabatic ascent. The climatological mean diabatic vertical velocity shows a region of local ascent at 60 km in the NH between $\sim 90^{\circ}\text{E}$ and $\sim 180^{\circ}\text{E}$ and at 65 km in the SH between $\sim 10^{\circ}\text{E}$ and $\sim 180^{\circ}\text{E}$. Local ascent atop the stratospheric anticyclones happens often enough at these locations that it is seen in the winter averages, despite the zonal mean polar winter descent at this latitude and altitude. This region of local ascent leads to a large cold pool between 68 km and 78 km that is directly below the region where MILs occur most often and forms the base of the MILs. The ascent-driven cold pool leads to enhanced atmospheric stability, thus decreasing vertical transport and mixing below the temperature inversion. The MIL forms above this region due to the strong vertical gradient in $d\theta/dt$ between 65 km and 80 km, with diabatic descent directly above diabatic ascent. It is this gradient that results in increasing temperatures in the mesosphere with height, overcoming the positive lapse rate. Above the MILs, the gradient in $d\theta/dt$ decreases between 80 km and 85 km, resulting in decreasing temperatures from the top of the MIL to the mesopause.

4. MIL Case Study

In this section we use WACCM to examine a MIL that formed on a typical January day above the Aleutian High, representative of the case study shown in Figure 2. The PW pattern during this MIL case study is similar to the case shown by Sassi *et al.* [2002, Figure 4], that showed westward tilting height anomalies in the stratosphere. On this day, upward propagating PWs lead to temperature anomalies that are in quadrature with the height anomalies [France and Harvey, 2013]. In the mesosphere the vortex and anticyclone do not tilt with height, suggesting that PWs are no longer propagating vertically. The temperature wave in the mesosphere is out of phase with the temperature wave in the stratosphere; a warm polar vortex is associated with gravity wave-driven descent and it is cold in the anticyclone. We examine the three-dimensional flow in the vicinity of a MIL and argue that local ascent above the anticyclone establishes a suitable background environment for MIL formation. We also consider the role of orographic and nonorographic gravity waves in producing the MIL.

Figure 6 shows polar plots of temperature (left) and $d\theta/dt$ (right) at the 3000 K potential temperature level (~ 60 km), which is near the base of the MIL where there is a temperature minimum. A MIL was detected at all longitudes and latitudes enclosed by the white contour. The anticyclone edge is shown in gray, and the polar

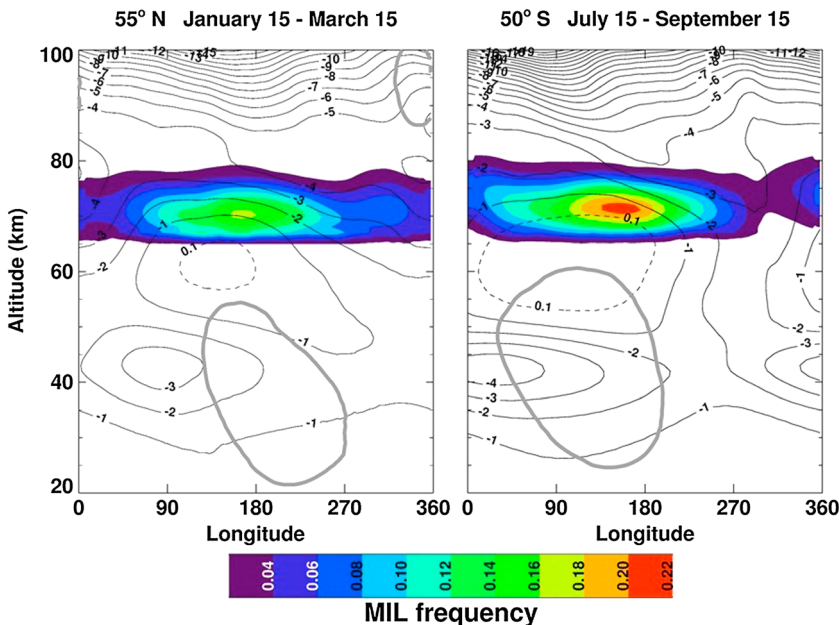


Figure 5. Forty year mean altitude-longitude sections of MIL frequency (left) from 50°N to 60°N between 15 January and 15 March and (right) from 40°S to 50°S between 15 July and 15 September. The altitude of the frequency contours indicates the base altitude of the inversions. MIL frequencies less than 2% are not colored. Thin solid and dashed contours indicate negative and positive $d\theta/dt$, respectively. The gray contour encompasses regions where the anticyclone occurs at least 10% of the time.

vortex edge is shown by the thick black contour in both plots. The thin black contours in Figure 6 (left) show the geopotential height of the theta surface; geostrophic flow is parallel to the geopotential height contours. In Figure 6 (right), diabatic vertical motion is contoured, with thin black contours indicating descent and thin white contours denoting ascent. Combining information from both panels shows clockwise flow and ascent in the anticyclone and counterclockwise flow and descent in the vortex. The ageostrophic flow, on the other hand, is perpendicular to the height contours, moving from higher heights to lower heights. This leads to convergence and diabatic descent in the vortex. Similarly, ageostrophic flow results in air moving away from the anticyclone, leading to divergence and adiabatic ascent and cooling. The cooling occurs near the base of the MIL at ~ 70 km and acts to enhance the inversion layer.

The vertical structure of the MIL is shown in Figure 7 as longitude-altitude (left) and latitude-altitude (right) sections that intersect the MIL on 18 January. The thin black and white contours show regions of diabatic descent and ascent, respectively. The anticyclones are indicated by the thick gray contours, and the vortex is shown by the thick black contours. White asterisks are superimposed at the top and bottom of identified MILs. The anticyclone and vortex tilt westward with height (left) up to ~ 70 km and the anticyclone tilts slightly poleward with altitude (right). The warm anomaly inside the anticyclone and along its western and northern flanks shows the warm stratopause and is at low altitudes due to ageostrophic descent [France et al., 2012]. There is a large cold anomaly at 70 km at the top of the anticyclone that spans 180° of longitude and 40° of latitude. Contours of diabatic vertical motion indicate local ascent colocated with the cold pool. This cold pool forms the base of the MIL, showing that local ascent atop the Aleutian High supports the MIL formation.

In order to more explicitly demonstrate the role of PWs in the formation of MILs, we use the method discussed in Salby et al. [2002]. Specifically, the lapse rate (Γ) can be separated into zonal mean ($\bar{\Gamma}$) and wave-driven (Γ') components

$$\Gamma = \bar{\Gamma} + \Gamma' \quad (1)$$

and is inversely proportional to the curvature of geopotential with height. For the wave-driven component, this is expressed by equation (5) from Salby et al. [2002]:

$$\Gamma' = -\frac{H}{R} \frac{\partial^2 \Phi'}{\partial z^2} \quad (2)$$

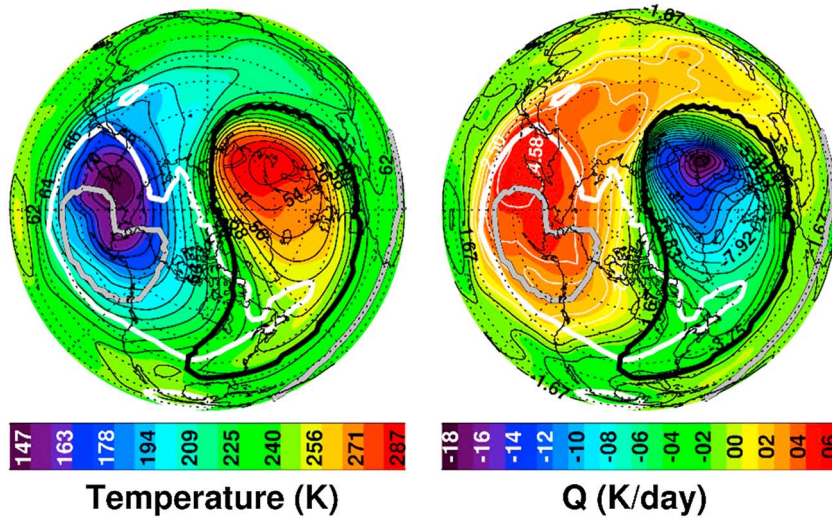


Figure 6. NH polar projections on 18 January of WACCM model year 6 at the 3000 K potential temperature surface (~60 km) showing (left) temperature (color) and geopotential height (thin black contours), and (right) $d\Phi/dt$ (color). Black and white contours (right) indicate regions of descent and ascent through the theta surface. In both panels, the thick white contour encompasses the region where a MIL is identified. Thick black and gray contours encompass regions where the vortex and anticyclones are present at this theta level, respectively. The Greenwich meridian is oriented to the right.

where H is the scale height, R is the specific gas constant for dry air (287 J/kg · K), and Φ is geopotential. The wave-driven component of the lapse rate is thus inversely proportional to the wave-driven geopotential anomalies. The PW-driven temperature anomalies are related to the lapse rate by

$$T' = \frac{H}{R} \frac{\partial \Phi'}{\partial z} \quad (3)$$

Figure 8 shows geopotential height anomalies (left) and the first (middle) and second (right) derivatives of the geopotential anomaly with respect to altitude, or T' and Γ' , respectively, for the same day shown in Figures 6 and 7. Note that geopotential height, rather than geopotential, anomalies are shown in Figure 8 (left). The middle and right panels are the first and second derivatives of geopotential anomalies with respect to altitude. Zonal wind is superimposed in Figure 8 (left) with the westerlies as solid contours, easterlies as dashed contours, and the zero wind line shown by the bold contour. The white symbols indicate the top and bottom of identified MILs. There are high geopotential anomalies colocated with the anticyclone and low anomalies with the vortex shown in Figure 7. The zero wind line is situated between the high and low geopotential anomalies, and this acts to filter stationary PWs and orographic gravity waves. On this day, orographic gravity wave breaking acts to weaken the westerlies by ~25 m/s/d to the west of the critical layer (not shown).

There is also a zero wind line that extends horizontally through the base of the MIL in Figure 8. Consistent with Sassi *et al.* [2002], WACCM shows focused momentum deposition by gravity waves as large as 100 m/s/d (not shown), which weaken the easterlies at the top of the anticyclone, leading to a zero wind line and an environment favorable for PW breaking. This results in geopotential anomalies that decay rapidly with height, causing $\frac{\partial \Phi'}{\partial z}$ to become negative above the anticyclone and, from equation (3), a cold anomaly that is colocated with bottom of the MILs between 120°E and 210°E. In order to have a PW-driven inversion, the wave-driven lapse rate must be sufficiently negative, causing rising temperatures with height. From equation (2), this occurs when the curvature is sufficiently positive. This is evident in the plot of the second derivative of geopotential with respect to height (right), where the highest values are within the MIL. Using equation (2) with scale height equal to 6 km, geopotential curvature values of 0.5 s^{-2} correspond to a wave-driven lapse rate of -10.5 K/km . This exceeds the magnitude of the dry adiabatic lapse rate and results in an inversion. Thus, we can conclude that the wave-driven geopotential anomalies and rapid decay with height directly contribute to the formation of MILs. It is interesting that the MIL observed on this day extends east of the region of positive curvature. This is likely due to warming associated with strong descent in the westward tilting vortex shown in Figure 7 (left).

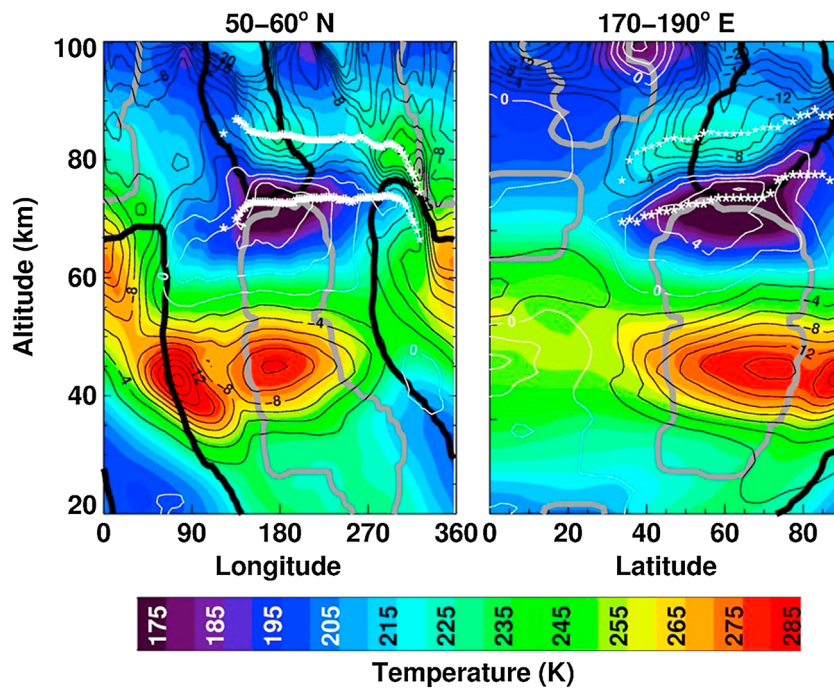


Figure 7. (left) Altitude-longitude section of WACCM temperature at 50–60°N and (right) altitude-latituden section of WACCM temperature at 170–190°E for the same model day as in Figure 6. Thin black and white contours are negative and positive $d\Phi/dt$ contours, respectively. The thick black and gray contours indicate where the vortex and anticyclones are identified on this day, respectively. White symbols indicate the top and bottom of identified MILs.

To further illustrate the role of decaying PWs in MIL formation, Figure 9 shows a climatological mean Hovmöller plot of the maximum curvature with height of the geopotential wave anomaly ($\frac{\partial^2 \Phi}{\partial z^2}$) at 55°N, between 65 km and 85 km (indicated by the color shading). Mean MLS data from 2004 to 2014 are shown in Figure 9 (left), and mean WACCM output for the 40 year run are shown in Figure 9 (right). The black contours indicate where MILs are present 30% of the time. The mean lapse rate is contoured in white. Positive regions

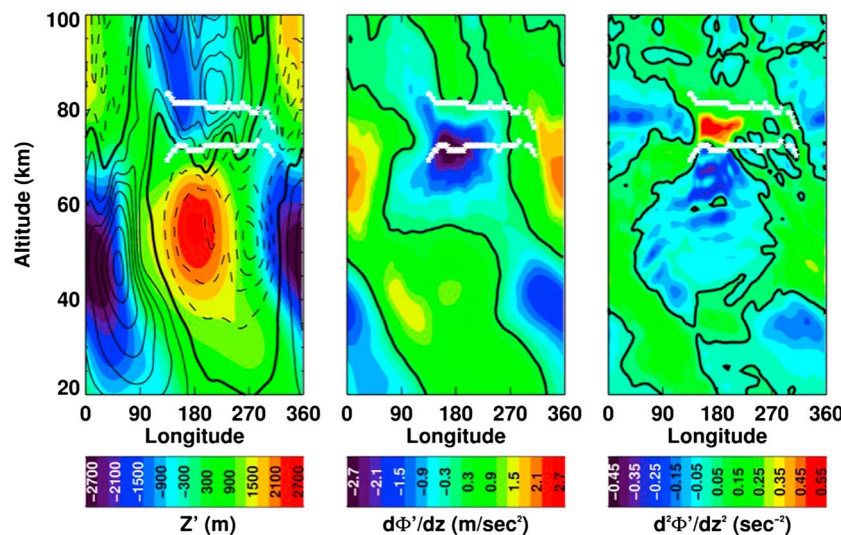


Figure 8. (left) Altitude-longitude sections at 55°N of eddy geopotential height (zonal mean removed), (middle) the first derivative of eddy geopotential with altitude, and (right) the second derivative of eddy geopotential with altitude (curvature) for the same day of WACCM output as in Figures 6 and 7. White symbols indicate the top and bottom of identified MILs. Black contours in Figure 8 (left) indicate the zonal mean wind, with thick, thin solid, and dashed lines indicating the zero wind line, westerly winds, and easterly wind, respectively. Wind contours are set at 20 m/s intervals.

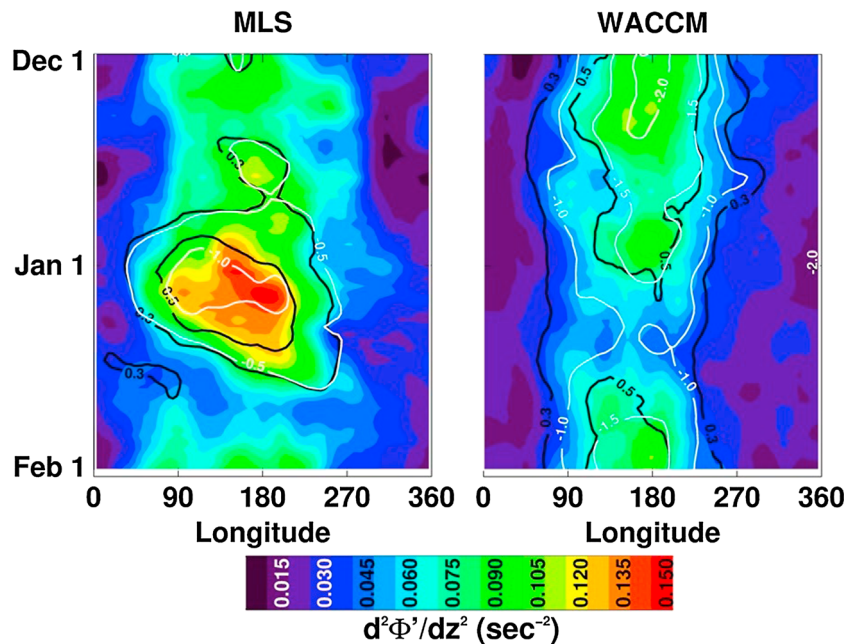


Figure 9. Hovmöller plots at 55°N of the average maximum eddy geopotential curvature between 65 km and 85 km (color) from 1 December to 1 February based on (left) 10 years of MLS data and (right) 40 years of WACCM output. Black contours indicate longitudes where MILs are identified 30% and 50% of the time at this latitude. White contours quantify the mean lapse rate of the temperature inversions.

of $\frac{\partial^2 \Phi'}{\partial z^2}$ are generally colocated with the location of MILs and regions of negative lapse rate. In MLS and WACCM, both MILs and regions of positive curvature occur preferentially between $\sim 90^\circ\text{E}$ and $\sim 270^\circ\text{E}$, with a maximum near the Date Line, consistent with Figure 2. That MIL frequency maximizes where $\frac{\partial^2 \Phi'}{\partial z^2} > 0$ suggests that the decay of PWs with height is a climatological driving mechanism of MILs. Notable differences between MLS and WACCM include largest curvature values and MIL frequencies near 1 January in MLS versus broad maxima in December and late January in WACCM. This may be due to the fact that PW activity is strongest during these respective months and is consistent with previous work that shows a peak in PW-driven stratospheric sudden warmings in WACCM during December [e.g., *de la Torre et al.*, 2012; *Holt et al.*, 2013] and during January in observations [*Charlton and Polvani*, 2007]. It is interesting that MLS shows comparable curvature in December to WACCM, though there are few MILs in MLS. In fact, the 0.3 MIL frequency contour in WACCM and MLS encompasses curvature values of $\sim 0.03 \text{ s}^{-1}$ and $\sim 0.08 \text{ s}^{-1}$, respectively, which suggests that the PW energy deposition required to produce a MIL frequency of 0.3 is nearly 3 times higher in MLS than in WACCM. This may be due to the known issue in WACCM with the background lapse rate being too small in the winter mesosphere [Smith, 2012]. This would then lead to less energy needed to reverse the temperature gradient and generate a MIL.

5. Conclusions

In this work, we present a climatology of long-lived extratropical winter MILs in WACCM, SABER, and MLS. We show that these MILs occur frequently over regions of anticyclonic flow where PWs decay rapidly with height. This occurs most often over the International Date Line near 55°N and 50°S, which are the locations of the Australian and Aleutian anticyclones, respectively. We show that wave-driven ascent and cooling in the mesosphere, combined with breaking and dissipating PWs, lead to the formation and enhancement of MILs. Because we have removed the diurnal tides and consider only long-lived (> 3 day) and large-amplitude ($> 12 \text{ K}$) MILs, our results indicate that PW-driven MILs extend up to 90 km.

Our findings are in agreement with *Sassi et al.* [2002], in that it demonstrates that middle to high latitude MILs form as a result of breaking PWs in the mesospheric surf zone. A difference between our work and theirs is that we show the maximum in NH midlatitude MIL frequency to be centered near the Date Line in both

WACCM and observations, while *Sassi et al.* [2002] show the maximum to be near 90°E. This could be simply due to the fact that their analysis is of lower latitude MILs near 43°N, while we consider latitudes between 50°N and 60°N.

We expand on previous work to show MIL statistics in the latest version of WACCM. Results show that PW-driven MILs occur climatologically above regions where there is positive curvature in geopotential anomaly with height in both WACCM and observations. This occurs because the decay of PWs with height induces a negative wave-driven component of the lapse rate above positive wave anomalies. When the wave-driven component of the lapse rate is sufficiently negative, an inversion occurs. This result demonstrates that PWs are a primary mechanism for MIL formation at middle to high latitudes and that WACCM properly simulates this mechanism. We made use of WACCM to demonstrate that there is vertical diabatic ascent and cooling near the base of the MIL, which acts to deepen the MIL. We also used WACCM to consider the role of gravity waves in producing MILs (not shown). We found that nonorographic gravity waves play an important role in creating the mesospheric surf zone by slowing the mean flow, which leads directly to PW breaking and subsequent MIL formation.

While WACCM MILs generally occur in the same geographic regions as MILs reported in satellite observations, WACCM tends to overestimate the frequency of MILs at middle to high latitudes. While the analysis here is focused on the winter months, we found that WACCM overestimates MILs at these latitudes in all seasons. This could be due to background temperatures in WACCM decreasing too slowly in the mesosphere, allowing MILs to form more easily [*Sica et al.*, 2007; *Smith*, 2012]. In the winter months, more PW forcing also likely contributes to a more robust mesospheric surf zone and larger MIL frequencies in WACCM than in observations.

Acknowledgments

The MERRA data used in this study have been provided by the Global Modeling and Assimilation Office (GMAO) at NASA Goddard Space Flight Center through the NASA GES DISC online archive and is available at disc.sci.gsfc.nasa.gov. We thank the MLS science team for processing and distributing the MLS data. We thank the SABER science team and Gats Inc. for processing and distributing the SABER data. MLS and SABER data used in this work are available at mls.jpl.nasa.gov and saber.gats-inc.com, respectively. WACCM output used in this work is available upon request from the corresponding author. This work was supported by several grants, including NASA NNX10AO54G, NNX09AG65G, NNX09AI04G, NNX14AH54G, NSF CEDAR AGS 0940124, and NSF ARC 1107498. The National Center for Atmospheric Research is supported by the National Science Foundation.

References

- Beres, J. H., R. R. Garcia, B. A. Boville, and F. Sassi (2005), Implementation of a gravity wave source spectrum parameterization dependent on the properties of convection in the Whole Atmosphere Community Climate Model (WACCM), *J. Geophys. Res.*, **110**, D10108, doi:10.1029/2004JD005504.
- Brasseur, G. P., J. T. Kiehl, J. Müller, T. Schneider, C. Granier, C. X. Tie, and D. Hauglustaine (1998), Past and future changes in global tropospheric ozone: Impact on radiative forcing, *Geophys. Res. Lett.*, **25**, doi:10.1029/1998GL900013.
- Chandran, A., R. L. Collins, R. R. Garcia, D. R. Marsh, V. L. Harvey, J. Yue, and L. de la Torre (2013), A climatology of elevated stratopause events in the whole atmosphere community climate model, *J. Geophys. Res. Atmos.*, **118**, 1234–1246, doi:10.1002/jgrd.50123.
- Charlton, A. J., and L. M. Polvani (2007), A new look at stratospheric sudden warmings. Part I: Climatology and modeling benchmarks, *J. Clim.*, **20**, 449–469, doi:10.1175/JCLI3996.1.
- Collins, R. L., G. A. Lehmacher, M. F. Larsen, and K. Mizutani (2011), Estimates of vertical eddy diffusivity in the upper mesosphere in the presence of a mesospheric inversion layer, *Ann. Geophys.*, **29**(11), 2019–2029, doi:10.5194/angeo-29-2019-2011.
- Cutler, L. J., R. L. Collins, K. Mizutani, and T. Itabe (2001), Rayleigh lidar observations of mesospheric inversion layers at Poker Flat, Alaska 65°N, 147°W, *Geophys. Res. Lett.*, **28**, 1467–1470, doi:10.1029/2000GL012535.
- Dao, P. D., R. Farley, X. Tao, and C. S. Gardner (1995), Lidar observations of the temperature profile between 25 and 103 km: Evidence of strong tidal perturbation, *Geophys. Res. Lett.*, **22**, 2825–2828.
- de la Torre, L., R. R. Garcia, D. Barriopedro, and A. Chandran (2012), Climatology and characteristics of stratospheric sudden warmings in the Whole Atmosphere Community Climate Model, *J. Geophys. Res.*, **117**, D04110, doi:10.1029/2011JD016840.
- Duck, T. J., and M. D. Greene (2004), High Arctic observations of mesospheric inversion layers, *Geophys. Res. Lett.*, **31**, L02105, doi:10.1029/2003GL018481.
- Duck, T. J., D. P. Sipler, J. E. Salah, and J. W. Meriwether (2001), Rayleigh lidar observations of a mesospheric inversion layer during night and day, *Geophys. Res. Lett.*, **28**(18), 3597–3600, doi:10.1029/2001GL013409.
- Fechine, J., C. M. Wrassé, H. Takahashi, M. G. Mlynczak, and J. M. Russell III (2008), Lower-mesospheric inversion layers over Brazilian equatorial region using TIMED/SABER temperature profiles, *Adv. Space Res.*, **41**, 1447–1453, doi:10.1016/j.asr.2007.04.070.
- France, J. A., and V. L. Harvey (2013), A climatology of the stratopause in WACCM and the zonally asymmetric elevated stratopause, *J. Geophys. Res. Atmos.*, **118**, 2241–2254, doi:10.1002/jgrd.50218.
- France, J. A., V. L. Harvey, C. E. Randall, M. H. Hitchman, and M. J. Schwartz (2012), A climatology of stratopause temperature and height in the polar vortex and anticyclones, *J. Geophys. Res.*, **117**, D06116, doi:10.1029/2011JD016893.
- Gan, Q., S. D. Zhang, and F. Yi (2012), TIMED/SABER observations of lower mesospheric inversion layers at low and middle latitudes, *J. Geophys. Res.*, **117**, D07109, doi:10.1029/2012JD017455.
- Garcia, R. R., and B. A. Boville (1994), Downward control of the mean meridional circulation and temperature distribution of the polar winter stratosphere, *J. Atmos. Sci.*, **51**, 2238–2245, doi:10.1175/1520-0469(1994)051<2238:COTMMC>2.0.CO;2.
- Garcia, R. R., D. R. Marsh, D. E. Kinnison, B. A. Boville, and F. Sassi (2007), Simulation of secular trends in the middle atmosphere, 1950–2003, *J. Geophys. Res.*, **112**, D09301, doi:10.1029/2006JD007485.
- Gent, P. R., et al. (2011), The Community Climate System Model Version 4, *J. Clim.*, **24**, 4973–4991, doi:10.1175/2011JCLI4083.1.
- Harvey, V. L., and M. H. Hitchman (1996), A climatology of the Aleutian High, *J. Atmos. Sci.*, **53**, 2088–2101.
- Harvey, V. L., R. B. Pierce, and M. H. Hitchman (2002), A climatology of stratospheric polar vortices and anticyclones, *J. Geophys. Res.*, **107**(D20), 4442, doi:10.1029/2001JD001471.
- Hauchecorne, A., M. L. Chanin, and R. Wilson (1987), Mesospheric temperature inversion and gravity wave breaking, *Geophys. Res. Lett.*, **14**, 933–936, doi:10.1029/GL014i009p00933.

- Haurwitz, B. (1961), Frictional effects and the meridional circulation in the mesosphere, *J. Geophys. Res.*, **66**, 2381–2391, doi:10.1029/JZ066i008p02381.
- Hitchman, M. H., J. C. Gille, C. D. Rodgers, and G. Brasseur (1989), The separated polar winter stratopause: A gravity wave driven climatological feature, *J. Atmos. Sci.*, **46**, 410–422.
- Holt, L. A., C. E. Randall, E. D. Peck, D. R. Marsh, A. K. Smith, and V. L. Harvey (2013), The influence of major sudden stratospheric warming and elevated stratopause events on the effects of energetic particle precipitation in WACCM, *J. Geophys. Res. Atmos.*, **118**, 11,636–11,646, doi:10.1002/2013JD020294.
- Hurrell, J. W., J. J. Hack, D. Shea, J. M. Caron, and J. Rosinski (2008), A new sea surface temperature and sea ice boundary dataset for the Community Atmosphere Model, *J. Clim.*, **21**(19), 5145–5153, doi:10.1175/2008JCLI2292.1.
- Irving, B. K., R. L. Collins, R. S. Lieberman, B. Thurairajah, and K. Mizutani (2014), Mesospheric Inversion Layers at Chathanika, Alaska (65°N, 147°W): Rayleigh lidar observations and analysis, *J. Geophys. Res. Atmos.*, **112**, doi:10.1002/2014JD021838.
- Kiehl, J. T., J. J. Hack, G. D. Bonan, B. A. Boville, B. P. Brieglab, D. L. Williamson, and P. J. Rasch (1996), Description of the NCAR Community Climate Model (CCM3), *NCAR Tech. Note NCAR/TN-420+STR*, 152 pp. [Available at <http://www.cgd.ucar.edu/cms/ccm3/TN-420/>.]
- Kinnison, D. E., et al. (2007), Sensitivity of chemical tracers to meteorological parameters in the MOZART-3 chemical transport model, *J. Geophys. Res.*, **112**, D20302, doi:10.1029/2006JD007879.
- Kumar, V. S., Y. B. Kumar, K. Raghunath, P. B. Rao, M. Krishnaiah, K. Mizutani, A. Aoki, M. Yasui, and T. Itabe (2001), Lidar measurements of mesospheric temperature inversion at a low latitude, *Ann. Geophys.*, **19**, 1039–1044, doi:10.5194/angeo-19-1039-2001.cd.
- Leblanc, T., and A. Hauchecorne (1997), Recent observations of mesospheric temperature inversions, *J. Geophys. Res.*, **102**(D16), 19,471–19,482, doi:10.1029/97JD01445.
- Liu, H., and M. E. Hagan (1998), Local heating/cooling of the mesosphere due to gravity wave and tidal coupling, *Geophys. Res. Lett.*, **25**(15), 2941–2944, doi:10.1029/98GL02153.
- Lin, S. J. (2004), A “vertically-Lagrangian” finite-volume dynamical core for global atmospheric models, *Mon. Weather Rev.*, **132**, 2293–2307.
- Lin, S. J., and R. B. Rood (1997), An explicit flux-form semi-Lagrangian shallow water model on the sphere, *Q. J. R. Meteorol. Sci.*, **123**, 2531–2533.
- Liu, H.-L., M. E. Hagan, and R. G. Roble (2000), Local mean state changes due to gravity wave breaking modulated by the diurnal tide, *J. Geophys. Res.*, **105**(D10), 12,381–12,396, doi:10.1029/1999JD901163.
- Livesey, N. J., et al. (2013), Earth Observing System (EOS) Microwave Limb Sounder (MLS) Version 3.3 and 3.4 Level 2 data quality and description document, Rep. JPL D-33509, Jet Propul. Lab., Pasadena, Calif.
- McFarlane, N. A. (1987), The effect of orographically excited gravity wave drag on the general circulation of the lower stratosphere and troposphere, *J. Atmos. Sci.*, **44**, 1775–1800.
- Meriwether, J. W., and C. S. Gardner (2000), A review of the mesosphere inversion layer phenomenon, *J. Geophys. Res.*, **105**, 12,405–12,416.
- Meriwether, J. W., and A. J. Gerrard (2004), Mesosphere inversion layers and stratosphere temperature enhancements, *Rev. Geophys.*, **42**, RG3003, doi:10.1029/2003RG000133.
- Meriwether, J. W., and M. G. Mlynczak (1995), Is chemical heating a major cause of the mesosphere inversion layer?, *J. Geophys. Res.*, **100**(D1), 1379–1387, doi:10.1029/94JD01736.
- Meriwether, J. W., X. Gao, V. B. Wickwar, T. Wilkerson, K. Beissner, S. Collins, and M. E. Hagan (1998), Observed coupling of the mesosphere inversion layer to the thermal tidal structure, *Geophys. Res. Lett.*, **25**, 1479–1482, doi:10.1029/98GL00756.
- Mertens, C., et al. (2001), Retrieval of mesospheric and lower thermospheric kinetic temperature from measurements of CO₂ 15 micron Earth limb emission under non-LTE conditions, *Geophys. Res. Lett.*, **28**(7), 1391–1394, doi:10.1029/2000GL012189.
- Mukhtarov, P., D. Pancheva, and B. Andonov (2009), Global structure and seasonal and interannual variability of the migrating diurnal tide seen in the SABER/TIMED temperatures between 20 and 120 km, *J. Geophys. Res.*, **114**, A02309, doi:10.1029/2008JA013759.
- Randall, C. E., V. L. Harvey, C. S. Singleton, P. F. Bernath, C. D. Boone, and J. U. Kozyra (2006), Enhanced NO_x in 2006 linked to strong upper stratospheric Arctic vortex, *Geophys. Res. Lett.*, **33**, L18811, doi:10.1029/2006GL027160.
- Randall, C. E., V. L. Harvey, D. E. Siskind, J. France, P. F. Bernath, C. D. Boone, and K. A. Walker (2009), NO_x descent in the Arctic middle atmosphere in early 2009, *Geophys. Res. Lett.*, **36**, L18811, doi:10.1029/2009GL039706.
- Ramesh, K., S. Sridharan, and S. Vijaya Bhaskara Rao (2013), Dominance of chemical heating over dynamics in causing a few large mesospheric inversion layer events during January–February 2011, *J. Geophys. Res. Space Physics*, **118**, 6751–6765, doi:10.1002/jgra.50601.
- Remsberg, E. E., et al. (2008), Assessment of the quality of the Version 1.07 temperature-versus-pressure profiles of the middle atmosphere from TIMED/SABER, *J. Geophys. Res.*, **113**, D17101, doi:10.1029/2008JD010013.
- Richter, J. H., F. Sassi, and R. R. Garcia (2010), Toward a physically based gravity wave source parameterization in a general circulation model, *J. Atmos. Sci.*, **67**(1), 136–156, doi:10.1175/2009JAS3112.1.
- Rienecker, M. M., et al. (2011), MERRA: NASA’s Modern-Era Retrospective Analysis for Research and Applications, *J. Clim.*, **24**, 3624–3648, doi:10.1175/JCLI-D-11-00015.1.
- Russell, J. M., III, M. G. Mlynczak, L. L. Gordley, J. Tansock, and R. Esplin (1999), An overview of the SABER experiment and preliminary calibration results, *Proc. SPIE Int. Soc. Opt. Eng.*, **3756**, 277–288.
- Salby, M. L. (1996), *Fundamentals of Atmospheric Physics*, pp. 188–189, Academic, San Diego, Calif.
- Salby, M. L., F. Sassi, P. Callaghan, D. Wu, P. Keckhut, and A. Hauchecorne (2002), Mesospheric inversions and their relationship to planetary wave structure, *J. Geophys. Res.*, **107**(D4), 4041, doi:10.1029/2001JD000756.
- Sassi, F., R. R. Garcia, B. A. Boville, and H. Liu (2002), On temperature inversions and the mesospheric surf zone, *J. Geophys. Res.*, **107**(D19), 4380, doi:10.1029/2001JD001525.
- Schmidlin, F. J. (1976), Temperature inversions near 75 km, *Geophys. Res. Lett.*, **3**, 173–176, doi:10.1029/GL003i003p00173.
- Schwartz, M. J., et al. (2008), Validation of the Aura Microwave Limb Sounder temperature and geopotential height measurements, *J. Geophys. Res.*, **113**, D15S11, doi:10.1029/2007JD008783.
- Sica, R. J., P. S. Argall, T. G. Shepherd, and J. N. Koshyk (2007), Model-measurement comparison of mesospheric temperature inversions, and a simple theory for their occurrence, *Geophys. Res. Lett.*, **34**, L23806, doi:10.1029/2007GL030627.
- Smith, A. K. (1996), Longitudinal variations in mesospheric winds: Evidence for gravity wave filtering by planetary waves, *J. Atmos. Sci.*, **53**, 1156–1173.
- Smith, A. K. (2003), The origin of stationary planetary waves in the upper mesosphere, *J. Atmos. Sci.*, **60**, 3033–3041.
- Smith, A. K. (2012), Global dynamics of the MLT, *Surv. Geophys.*, **33**, 1177–1230, doi:10.1007/s10712-012-9196-9.
- States, R. J., and C. S. Gardner (1998), Influence of the diurnal tide and thermospheric heat sources on the formation of mesospheric temperature inversion layers, *Geophys. Res. Lett.*, **25**, 1483–1486, doi:10.1029/98GL00850.
- States, R. J., and C. S. Gardner (2000), Thermal structure of the mesopause region (80–105 km) at 40°N latitude. Part I: Seasonal variations, *J. Atmos. Sci.*, **57**, 66–77.

- Wallace, J. M., and P. V. Hobbs (1977), *Atmospheric Science: An Introductory Survey*, Academic, San Diego, Calif.
- Waters, J. W., et al. (2006), The Earth Observing System Microwave Limb Sounder (EOS MLS) on the Aura satellite, *IEEE Trans. Geosci. Remote Sens.*, **44**, 1075–1092.
- Whiteway, J. A., A. I. Carswell, and W. E. Ward (1995), Mesospheric temperature inversions with overlying nearly adiabatic lapse rate: An indication of a well-mixed turbulent layer, *Geophys. Res. Lett.*, **22**, 1201–1204, doi:10.1029/95GL01109.
- Wu, Q., et al. (2008), Global distribution and interannual variations of mesospheric and lower thermospheric neutral wind diurnal tide: 1. Migrating tide, *J. Geophys. Res.*, **113**, A05308, doi:10.1029/2007JA012542.
- Xu, J., A. K. Smith, H.-L. Liu, W. Yuan, Q. Wu, G. Jiang, M. G. Mlynczak, J. M. Russell III, and S. J. Franke (2009), Seasonal and quasi-biennial variations in the migrating diurnal tide observed by Thermosphere, Ionosphere, Mesosphere, Energetics and Dynamics (TIMED), *J. Geophys. Res.*, **114**, D13107, doi:10.1029/2008JD011298.
- Zhang, X., J. M. Forbes, M. E. Hagan, J. M. Russell III, S. E. Palo, C. J. Mertens, and M. G. Mlynczak (2006), Monthly tidal temperatures 20–120 km from TIMED/SABER, *J. Geophys. Res.*, **111**, A10S08, doi:10.1029/2005JA011504.

ERRATUM

In the originally published version of this article, the second to last sentence in the acknowledgements section was erroneous. This error has since been corrected and this version may be considered the authoritative version of record.